Precision Mechanical Rotation Sensors for Terrestrial Gravitational Wave Observatories

M. P. Ross

A dissertation
submitted in partial fulfillment of the
requirements for the degree of

Doctor of Philosophy

University of Washington

2019

Reading Committee:

Name of Chairperson, Chair

First committee member

Next committee member

etc

Program Authorized to Offer Degree:
Physics

University of Washington

Abstract

Precision Mechanical Rotation Sensors for Terrestrial Gravitational Wave Observatories

M. P. Ross

Chair of the Supervisory Committee:
Title of Chair Name of Chairperson
Department of Chair

TABLE OF CONTENTS

Page

List of Figures iii

Chapter 1: Introduction 1
- 1.1 Gravitational Wave Theory 1
  - 1.1.1 Linearized General Relativity 1
  - 1.1.2 Compact Binary Coalescence 2
- 1.2 LIGO 3
  - 1.2.1 Sensitivity 3
  - 1.2.2 Events 4
- 1.3 Seismic Isolation 5

Chapter 2: 1-m Scale Ground Rotation Sensors 6
- 2.1 Tilt Contamination 6
- 2.2 Sensor Correction with Tilt Subtraction 8
- 2.3 Mechanical System 9
- 2.4 Multi-Slit Autocollimator Readout 9
- 2.5 Controls 12
- 2.6 Noise Performance 13
- 2.7 Hanford Installation 14
- 2.8 Livingston Installation 18

Chapter 3: 30-cm Scale On-Board Rotation Sensors 19
- 3.1 Angular Controls 19
- 3.2 Isolation Scheme 20
- 3.3 Mechanical System 21
- 3.4 Interferometric Readout 22
- 3.5 Mass Adjustment 24

3.6 Controls 24
3.7 Noise Performance 25

Chapter 4: Applications 26
4.1 Geophysics 26
4.1.1 Rayleigh Wave Theory 26
4.1.2 Wave Field Parameter Extraction 27
4.1.3 Single Station Dispersion Measurements 28
4.2 Newtonian Noise 30
4.2.1 Theory 30
4.2.2 Observations 30

LIST OF FIGURES

Figure Number Page

2.1 7
2.2 10
2.3 Noise budge for the Beam Rotation Sensors where the blue curve shows the performance at a quiet time, in red is the motion of the reference mirror which can be regarded as an estimate of the readout noise, yellow shows an estimate of the thermal noise, purple shows the noise from the capacitive actuators, and green shows the some of all known noise sources. 15
2.4 16
2.5 17
2.6 17

3.1 20
3.2 21
3.3 22
3.4 23

4.1 **cite tilt seismology** 29
4.2 30

DEDICATION

To Grace

Chapter 1

INTRODUCTION

1.1 Gravitational Wave Theory

1.1.1 Linearized General Relativity

In early twentieth century, Einstein formulated the theory of General Relativity, which supplanted the static space-time in which all prior physics was formulated in, with a deformable space-time which gave a geometric explanation for gravity. This space-time is described by a unitless tensor field, $g_{\mu\nu}$, called the metric [**?**]. The deformation of this metric follows the Einstein equation:

$$R_{\mu\nu} - \frac{1}{2}R\ g_{\mu\nu} + \Lambda g_{\mu\nu} = \frac{8\pi G}{c^4}T_{\mu\nu} \tag{1.1}$$

where $R_{\mu\nu}$ is the Riemann tensor, R is the Ricci scalar, Λ is the cosmological constant, G is the gravitational constant, c is the speed of light, and $T_{\mu\nu}$ is the stress energy tensor.

If one focuses on a locally flat region of space which is much smaller than the scale of the universe, then the cosmological constant term can be sent to zero and the metric can be approximated via [**?**]:

$$g_{\mu\nu}(\vec{x}, t) \approx \eta_{\mu\nu}(\vec{x}, t) + h_{\mu\nu}(\vec{x}, t) \tag{1.2}$$

where $\eta_{\mu\nu}$ is the flat Minkowski metric and $h_{\mu\nu}$ is a small perturbation[1], $|h_{\mu\nu}| \ll 1$. Applying the Einstein equation and transferring to a transverse-traceless coordinate system yields the wave equation:

$$\Box h_{\mu\nu} = -\frac{16\pi G}{c^4}T_{\mu\nu} \tag{1.3}$$

[1] The largest amplitude of gravitational wave strain measured thus far is on the order of $|h_{\mu\nu}| \approx 10^{-21}$[**?**]

For a complete derivation see Reference [?]. Vacuum solutions propagating along the z-axis can readily be found as:

$$h_{ij}(t,x) = \begin{pmatrix} h_+ & h_\times & 0 \\ h_\times & -h_+ & 0 \\ 0 & 0 & 0 \end{pmatrix} \cos\left(\omega t - \kappa z\right) \tag{1.4}$$

where h_+ and $h_\times$ are the amplitudes in the "plus" and "cross" polarizations[2], ω is the angular frequency of oscillation, and κ is the wavenumber. Here i and j run from 1 to 3 and correspond to the the three spacial coordinates. The time components are suppressed as the $h_{0\nu}$ components are zero due the coordinate choice and h_{00} is zero outside the source.

1.1.2 Compact Binary Coalescence

As of writing, the only systems to have been observed to emit gravitational waves are composed of two compact[3] objects orbiting a common center of mass, so called compact binaries. These objects could be neutron stars, as with the Hulse-Taylor binary pulsar[?] and GW170817[?], or black holes like GW150914[?] and most events in the GWTC-1[?].

Such a system can be treated as two point masses, $m_{1,2}$ in a Keplerian orbit which decays due to the emission of gravitational waves. The gravitational waves emitted by such a system can be shown to be:

$$h_+(t) = \frac{4}{r}\left(\frac{GM}{c^2}\right)^{5/3}\left(\frac{\pi f}{c}\right)^{2/3}\frac{1+\cos^2\theta}{2}\cos(\omega t + \phi) \tag{1.5}$$

$$h_\times(t) = \frac{4}{r}\left(\frac{GM}{c^2}\right)^{5/3}\left(\frac{\pi f}{c}\right)^{2/3}\cos\theta\sin(\omega t + \phi) \tag{1.6}$$

---

[2] A massless graviton is assumed here. A massive graviton would yield five polarizations instead of two. Current graviton mass constraints are $m_g < 7.7 \times 10^{-23} eV/c^2$ [?]

[3] The compactness of the objects are importance only to satisfy a point mass approximation and to allow observation in current instruments. Non-compact objects such as white and brown dwarfs will emit gravitational waves in their inspiral phase but merge due to Roche lobe overflow long before entering the frequency band accessible today.

where $M = (m_1 m_2)^{3/5}/(m_1 + m_2)^{1/5}$ is the chirp mass, r is the distance to the center of mass of the source, θ is the viewing angle, $f = \omega/2\pi$ is the frequency of oscillation, and ϕ is the initial phase of the system.

The emission of these gravitational waves carry energy away from the system and thus the orbit decays. As the radius of the orbit decreases the frequency of oscillation must grow due to Kepler's law. This then causes the amplitude of the emitted gravitational waves to grow and the orbit to decay quicker. The frequency change during this run away process can be shown to be:

$$\dot{f} = \frac{96}{5}\pi^{8/3}\left(\frac{GM}{c^3}\right)^{5/3} f^{11/3} \tag{1.7}$$

This process produces a characteristic "chirp" signal which begins as low frequency and amplitude then grows in amplitude while shifting to higher frequency. The signal culminates in a final sharp increase in both frequency and amplitude before the objects merger. This can be seen in Figure **??** which shows a spectrogram of the observed strain at the LIGO observatories for GW170817.

include figure of GW170817

Although binary systems are the topic of choice here, many other systems should theoretically emit gravitational waves. These can range from asymmetric spinning stars and supernova to cosmic strings and density perturbations in the early universe. With the measurement of gravitational waves, humankind technologically expand our senses to include the faint vibrations of space-time. This ability has expanded the types of astronomical systems we can study and may one day allow further insight into the beginning of the universe.

1.2 LIGO

1.2.1 Sensitivity

The Laser Interferometric Gravitational wave Observatory (LIGO) is a pair of 4 km long L-shaped interferometric gravitational wave detectors, one located in Hanford, Washington (LHO) and the other in Livingston, Louisiana. Each observatory is a dual-recycled Fabry-

Perot Michelson interferometer which measures the differential strain between its two arms formed by pairs of partially reflective mirrors, also called test masses.

include LIGO schematic

As a gravitational wave passes the observatory, the arms experience a strains that follow [**?**]:

$$h_{xx} = h_+ \left(\cos^2\theta\ \cos^2\phi - \sin^2\phi\right) + 2\ h_\times\ \cos\theta\ \sin\phi\cos\phi \tag{1.8}$$

$$h_{yy} = h_+ \left(\cos^2\theta\ \sin^2\phi - \cos^2\phi\right) - 2\ h_\times\ \cos\theta\ \sin\phi\cos\phi \tag{1.9}$$

$$h = \frac{1}{2}\left(h_{xx} - h_{yy}\right) = \frac{1}{2}h_+\ \left(1 + \cos^2\theta\right) + h_\times\ \cos\theta\ \sin 2\phi \tag{1.10}$$

where h_{xx} and h_{yy} are the strain along the x and y arm respectively, θ and ϕ are the polar and azimuthal angles of the direction of propogation, and h is the differential strain as measured by the observatory.

The complex series of optics allows the observatory to measure differential strains down to 10^{-23} **at 40 Hz**. A noise curve for **some** observatory is shown in Figure **??** where one can see that the sensitive band of the observatory runs from **30 Hz up to 16 kHz**. At low frequencies the noise is dominated by residual control noise while at high it is dominated by noise caused by quantum fluctuations.

include LIGO strain curve

1.2.2 Events

With the current sensitivity the primary systems of interest are compact binaries, discussed in Section 1.1.2, which merger within the band of interest. A equal mass 200 $M_\odot$ binary black hole system would merger at **11 Hz** while a 1.4 $M_\odot$ binary neutron star system mergers at **1.5 kHz** yet emits appreciably while sweeping through the LIGO band.

During the first and second observing runs of LIGO, ten binary black hole systems and one binary neutron star merger were detected with high significance. The black holes ranged from 7 $M_\odot$ **to** 120 $M_\odot$ and merged at distances from **100 Mpc to 2 Gpc**. The neutron star binary was composed of a 1.2 $M_\odot$ **and a** 1.4 $M_\odot$ at **1 Mpc**. These systems are tabulated in Table **??**.

Event Table

The ongoing third observing run has had # significant candidates: # binary black holes, # binary neutron stars, and # black hole neutron star systems. Although these candidates have not been verified to be true gravitational wave events i

1.3 Seismic Isolation

Chapter 2

1-M SCALE GROUND ROTATION SENSORS

2.1 Tilt Contamination

At their core seismometers are low frequency spring mass system which measures the difference in motion between the casing and the device's proof mass. Above the resonant frequency of the spring mass system, this allows for accurate measurements of the motion in reference to an inertial frame of any object that the casing is rigidly connected to, be it the ground or a suspended table. Over the past **some time** this technology has produced devices that are sensitive to **number and range**. However, these systems are fundamentally susceptible to any stray forces acting on the proof mass.

Of interest here is the contamination due to the rotation of the device within a external gravitational field, namely the field caused by the earth. The rotation in respect to a fixed gravitational force will be referred to as tilt.[1] From the proof mass's frame, a tilt is equivalent to a rotation of the gravitational force. This yields a horizontal acceleration of the proof mass of:

$$a = g \sin(\theta)$$

where g is the gravitational acceleration on the surface of the earth and θ is the angle that the device is rotated. This acceleration adds a second term to the seismometer's output shown below for small angles and in the Fourier domain:

$$\tilde{x}_{seis}(\omega) = \tilde{x}_{trans}(\omega) + \frac{g}{\omega^2}\tilde{\theta}_{wind}(\omega)$$

[1] Although a subtle difference, the distinction would be of great consequences if the local gravitational field was varying rapidly. In that case the sensors described here would be of little use as they are rotational sensors not tilt sensors.

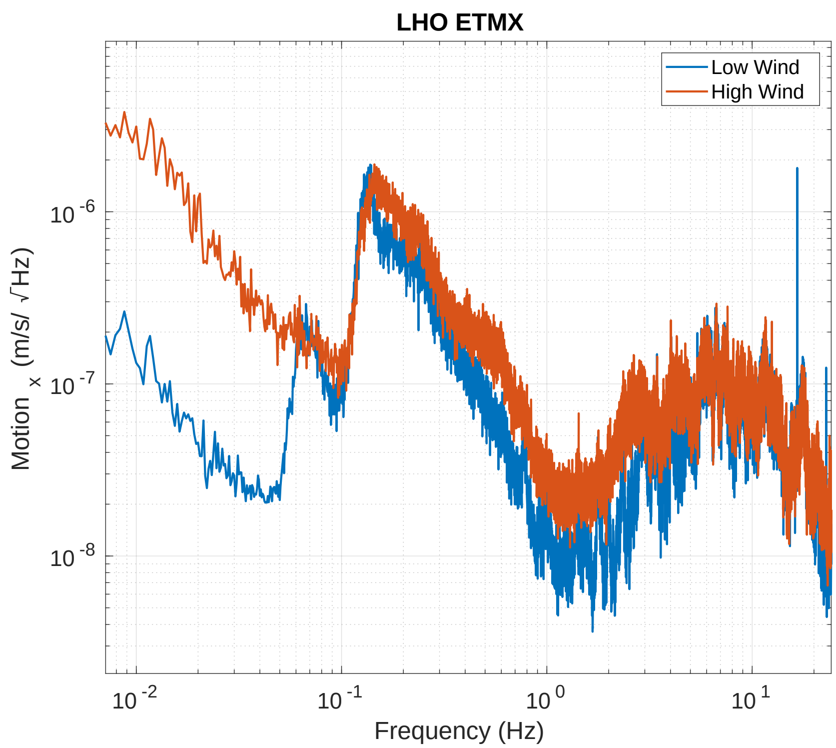

Figure 2.1

where x_{seis} is the seismometer's output, x_{trans} is the translational motion of the device, and ω is the frequency at which the tilt is being driven.

With this additional contribution, it becomes immediately clear that, for a given amplitude of tilt, the contamination term contributes more at lower frequencies and readily dominates the translational signal. In the context of the ground seismometers at the observatory, the tilt signal swamps the translational component below $\sim$ 100 mHz. Above which the seismometer signal is dominate by the ever present oceanic microseism which is driven by low frequency pressure waves with the ocean and their interaction with the shoreline. **CITE** This can be seen in Figure 2.1 which shows an amplitude spectral density of a ground seismometer at LHO during both low and high wind conditions.

The dominate driver of ground tilts at the observatories is wind acting on the walls of the building. Although one would naiively assume that the wind would rigidly rotate the building, it was found that the true mechanism is differential pressure acting on the walls deforms the building's concrete slab. **cite?**

2.2 Sensor Correction with Tilt Subtraction

There are a few different ways to combat such a contamination. The most straight forward is to decrease the wind pressure by designing builds that don't interact with the wind as much or installing wind blocks such as wind fences or earth burms. Both of these option require significant construction and for the case of LIGO, tilt contamination was not known to be a problem when design the observatories. Another option is to build seismometers that are suspended in such a way that they do not experience tilts. This is an active area of research and may yield tilt-free seismometers. **cite**

The scheme that will be used here is to measure the tilt with an independent rotation sensor and subtract the wind driven contribution. This would then yield a channel of the following form:

$$x_{seis}(\omega) = x_{trans}(\omega) + \frac{g}{\omega^2}\theta_{wind}(\omega) \tag{2.1}$$

$$- \frac{g}{\omega^2}\theta_{meas}(\omega) \tag{2.2}$$

where θ_{meas} is the tilt seen by the rotation sensor. Given a coherence γ between the tilt component of the seismometer and rotation sensors this yields the following: **CHECK math**

$$x_{seis}(\omega) = x_{trans}(\omega) + \frac{g}{\omega^2}(1-\gamma)\theta_{wind}(\omega)$$

This is then a low tilt channel which can be used within the LIGO seismic isolation system.

2.3 Mechanical System

The Beam Rotation Sensor (BRS) is a beam balance comprised of a 1-m long beam hung from two 10-15 μm thick beryllium-copper flexures. Figure 2.2 shows a CAD model of the beam balance.

This design makes the beam stiff in all degrees of freedom other than rotations around the horizontal axis which intersects the two flexure pivot points. This forms a system consisting of two elementary subsystems: a rotational spring mass system formed by the stiffness of the flexures, and a simple pendulum due to the offset of the pivot point and the center of mass. This is then described by the following equation of motion: [18]

$$I\ddot{\theta}(t) + \kappa(1 + \frac{i}{Q})(\theta(t) - \theta_p(t)) + Mg\delta\theta(t) + M\delta\ddot{x}_p(t) = \tau_{ex}(t)$$

where θ and θ_p are, respectively, the angle of beam and the platform with respect to gravitational vertical, τ_{ext} is the sum of all exterior torques, I is the moment of inertia, Q is the quality factor of the system, κ is the spring constant of the flexures, M is the mass of the balance, g is the gravitational acceleration, δ is the vertical distance from the center of mass and the pivot point, and x_p is the translation of the platform.

derive translational coupling and readout equation

In ideal operation, one would tune the center of mass to be at the pivot point and thus would produce a pure rotational spring-mass system with no translational coupling. In this limit, the rotation sensor is a rotational analog to a seismometer; above the resonant frequency as the casing rotates the beam stays inertial and thus allows one to measure the casing's rotation.

2.4 Multi-Slit Autocollimator Readout

Optical levers are a simple optical angular readout which exploits the law of reflection to measure angular deflections of a mirror by observing the displacement of a reflected beam.

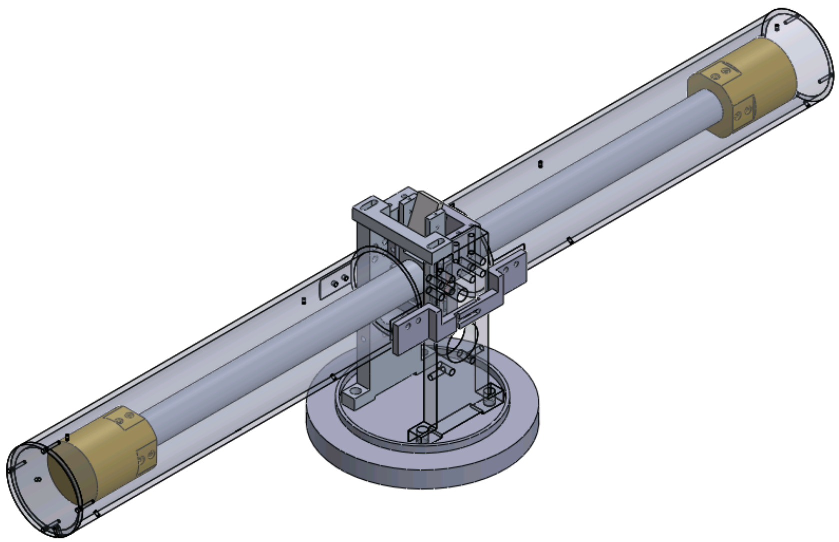

(a)

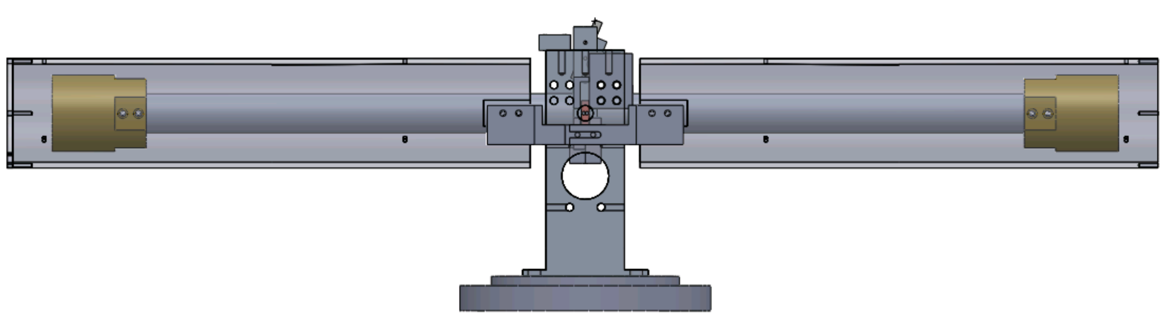

The angle of the mirror is then described as:

$$\theta_{mirror} = \frac{x_{reflected}}{2d}$$

where θ_{mirror} is the angle of the mirror, $x_{reflected}$ is the displacement of the reflected beam, and d is the distance between the optical system and the mirror. This allows one to increase the precious of the angular measurements arbitrarily by increasing d. However, with this comes a few disadvantages. One the effective gain of the sensor depends of the d which may not be well known. Additionally, the system is sensitive to changes in d.

An autocollimator adds a lens located one focal length from light source and the screen, shown in Figure **number**. This effectively replace the distance dependence with the focal length of the lens which allows the system to be only sensitive, to first order, to the angular motion of the mirror.

autocollimator schematic

To improve upon this further, a partially reflective mirror can be placed in between the optical system and the main mirror to act as a reference and allows for the subtraction of any motion of the optical system with respect to the main mirror. This yield a angular readout described by:

$$\theta_{mirror} = \frac{x_{main} - x_{reference}}{2f}$$

where f is the focal length of the lens and $x_{reference}$ is the beam spot from the reference mirror.

make table of BRS autocollimator parameters: focus, number of slits, slit width, CCD type, light source, frequency

An increase in sensitivity can be made by employing a multi-slit autocollimator [2]. This consists of an autocollimator with the light source replaced by a illuminated photomask of a number of thin slits. The pattern is then reflected off a set of reference and main mirror and imaged by a line CCD camera. These images are then analyzed to measure the distance between them thus yielding a measurement of angle. For the BRSs, this image analysis is achieved using bespoke software written in C# which can be found at www.github.com/mpross/BRSReadout

To extract the distance between the patterns, the image goes through a series of steps to go from a vector of pixel intensities to a single angular output. When the software begins, the first frame that is captured is saved. All future frames are split into two, with one part representing the reference mirror and the other the main mirror. The cross correlation is then taken between each part and it's matching part from the first frame. This gives a curve who's maximum is located at the pixel number corresponding to separation between the pattern in the current frame and the first frame, which can be seen in Figure **number**. The points of this curve that are near the maximum are then fit to a Gaussian which allows for the extraction of the location of the peak with sub-pixel resolution. This is done for each pattern separately after which the difference between the reference pattern location and the main pattern location is taken. The difference is then proportional to the change in angle between the casing and the beam.

Compared to previous image analysis algorithms [**?**], this algorithm is more computationally efficient while also being less susceptible to variations in the pattern image due to dust particulate, incorrect focusing, or beam clipping. A sensitivity of $\sim$ **0.1 nrad/$\sqrt{\text{Hz}}$** was achieved with this autocollimator design and image analysis algorithm.

2.5 Controls

As the BRSs are installed in active lab spaces, anthropogenic actively and environmental disturbances regularly apply torques on the beam balance, either through mechanical coupling through the flexures or gravitational coupling with the end masses. These can then cause the motion at the resonant frequency to rise to undesirable amplitudes. As the beam motion increases so does the noise. Additionally, some disturbances can be large enough to cause the amplitude to exceed the dynamic range of the autocollimator readout system.

The alleviate this issue, capacitor plates are installed underneath each end of the beam balance to act as actuators. The force between the two capacitor plates follows the following:

$$F = \frac{\epsilon A V^2}{2d^2} \tag{2.3}$$

where ϵ is the permittivity of the material between the plates, A is the area of the plate, V is the voltage applied to the plates, and d is the distance between the plates. The plate under the beam is connected to a DAC while the beam is grounded which allows for a controlled actuation torque to be applied to the beam.

The control scheme that was adopted was one in which the feedback signal that is sent to the capacitors is the angular velocity of the beam band passed between 2 mHz and 20 mHz to include only motion at frequencies near the resonance. The feedback is additionally applied with low gain so that the feedback is only adding loss to the system as compared to locking the system in a strong feedback loop where all of the motion is absorbed into the control system. This is then implemented with two gain stages, a "low amplitude" stage which is always on and yields a Q of 10-15 and a "high amplitude" stage which is triggered if the amplitude rises above a threshold that is set based on the behavior of the given device and gives a Q of **number**.

2.6 Noise Performance

In addition to the 0.1 nrad/$\sqrt{\text{Hz}}$ white noise of the autocollimator readout, these devices suffer from a various mechanical noise sources, namely noise due to temperature variations and due to the thermal motion of the flexures.

Although the exact physical mechanism is unknown at this juncture, it has been observed that variations in the exterior temperature cause shifts in the balance's equilibrium position. Furthermore, temperature gradients across the instrument emanating from unbalanced heat sources and air currents have been seen to cause time varying noise. To alleviate this issue the instrument's vacuum chamber and optics are wrapped in multiple alternating layers of packing foam and aluminum foil. The entire apparatus is then placed inside a large double walled insulation box to further decrease any temperature variations. This eliminates this as a dominate noise source unless the room in which the instrument is housed undergoes large temperature variations.

More limiting is the noise due to the thermal vibrations of the flexure. At any non-zero temperature, a portion of the thermal energy of the flexures is stored in the vibrational modes of the flexure. This causes a fundamental stochastic noise floor that goes as such: **add thermal noise equation** Since this noise source enters as a torque on the beam balance, it is filtered by the harmonic response making it fall as $1/f^2$ above the resonant frequency. To limit the influence on the performance of the device, the resonant frequency of the spring mass system is pushed to the lowest frequency that is mechanically feasible.

One further noise source that acts on the beam balance comes from voltage noise on the capacitive actuators. The force caused by the follows Equation 2.3 and can be shown to be sub dominate.

The noise budget for a BRS is shown in Figure 2.3 which shows that the device is readout dominated above ~20 mHz and below is dominated by thermal noise. An excess in the measured noise can be seen below 3 mHz which is believed to be due to residual temperature noise. Respectively at 150 mHz, 3 Hz, and 6 Hz the rotational microseism, torsion mode of the beam balance, and motion due to nearby instrumentation can be seen above the predicted noise sources.

2.7 Hanford Installation

Between the first (O1) and second (O2) observing runs of LIGO, two BRSs were installed at the LIGO Hanford Observatory, one at each end station correcting the translations along their respective arm. Although one would expect that the corner station sensors would also need to be corrected, a location was found within the corner station building which exhibited low tilt. **cite** This is thought to be due to the shape of the building the distance between this location and the walls. As such no BRS was necessary to achieve low tilt injection seismic isolation.

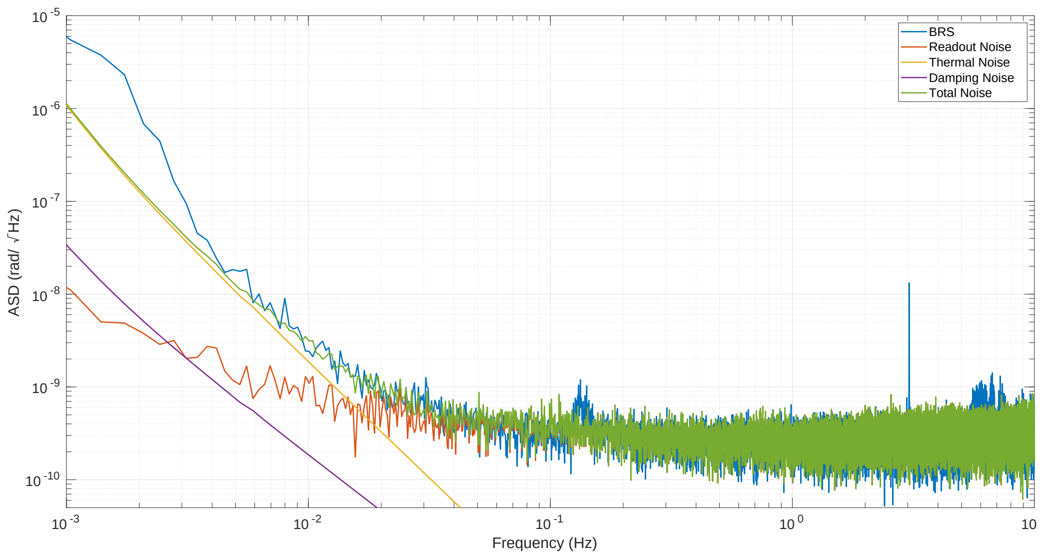

Figure 2.3: Noise budge for the Beam Rotation Sensors where the blue curve shows the performance at a quiet time, in red is the motion of the reference mirror which can be regarded as an estimate of the readout noise, yellow shows an estimate of the thermal noise, purple shows the noise from the capacitive actuators, and green shows the some of all known noise sources.

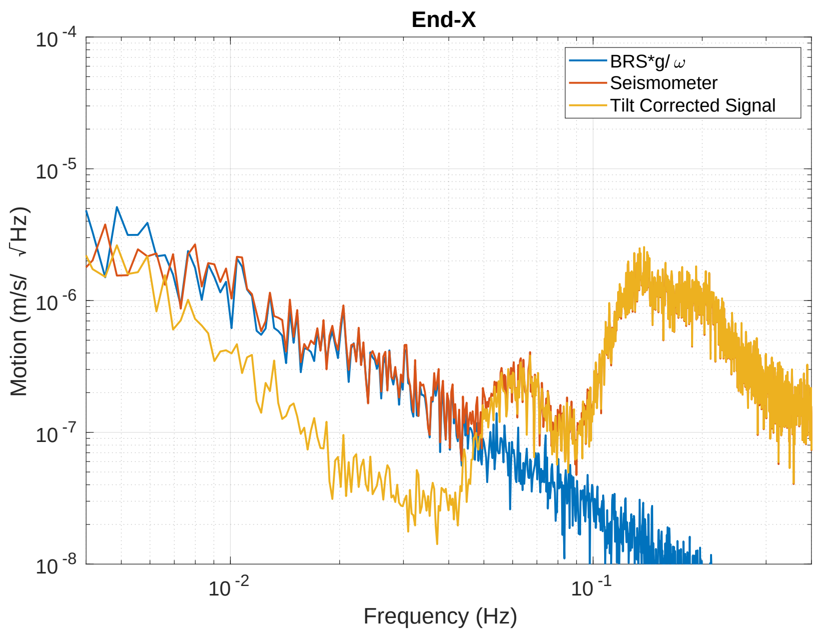

Figure 2.4

The tilt subtraction performance achieved with these devices can be seen in Figure 2.4 where it is evident that the system achieves tilt subtraction from around 6 mHz to 50 mHz. Above 50 mHz the seismometer signal is dominated by the oceanic microseism and the tilt contribution is negligible. Below 6 mHz, the BRS signal becomes overwhelmed by instrumental noise. This performance can also be seen in Figure 2.5 which shows a example time series of the tilt subtraction.

This tilt subtracted channel was then used as the ground signal for the isolation's sensor correction instead of the raw seismometer. Along with the use of the low tilt seismometer for the corner station, the addition of the BRSs in the seismic control scheme yielded significant improvements in the ability to lock the interferometer at increased wind speeds which can be seen in Figure 2.6

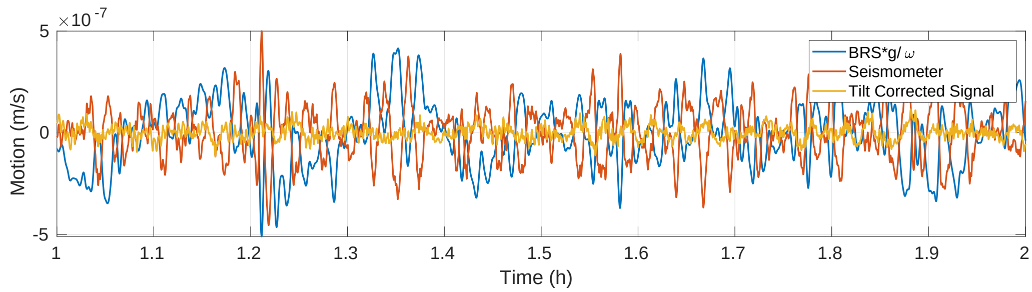

Figure 2.5

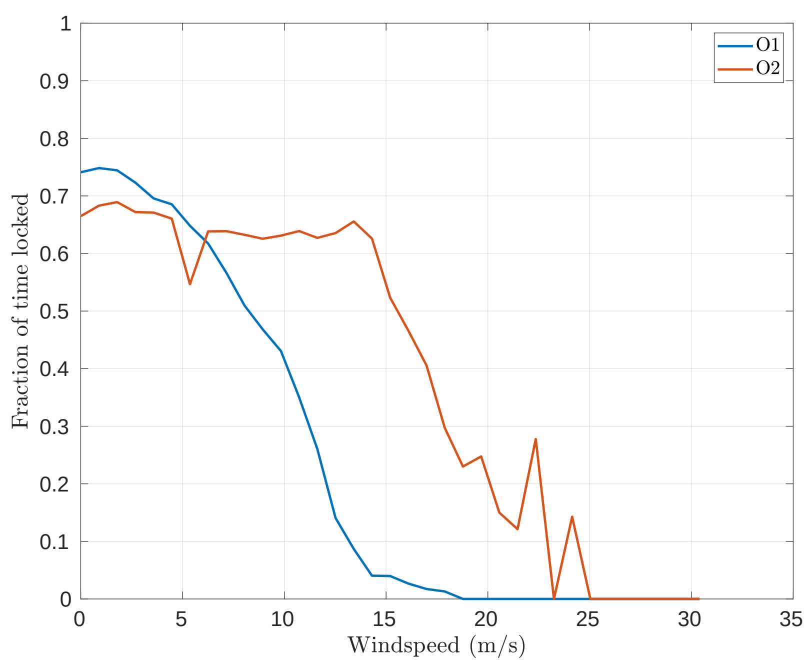

Figure 2.6

2.8 Livingston Installation

After the success of the Hanford BRS installation, four devices were installed at the LIGO Livingston Observatory (LLO) between the second and third (O3) observing runs. Due to differences in the size and shape of the corner station building at LLO a low tilt location was not found. Thus two BRSs were installed located near the two input test masses (ITM) correcting the seismometer signal oriented along their respective arms.

All four were implemented in a similar fashion as the Hanford devices.

Chapter 3

30-CM SCALE ON-BOARD ROTATION SENSORS

3.1 Angular Controls

To operate the LIGO interferometers in their optimal configuration, the angular motion of the test masses in the pitch degree of freedom must be under **number** nrad/$\sqrt{\text{Hz}}$ at **number** Hz where as the ground rotates at ∼**number** nrad/$\sqrt{\text{Hz}}$ at **number** Hz. To achieve this desired performance, the seismic isolation operated in the rotational degrees of freedom as well as the translation. Additionally, the upper three masses of the quadruple pendulum are actively actuated at frequencies between **number** and **number** Hz to decrease any residual motion.

With the current system, at **number** Hz the seismic isolation is limited by the sensor noise in the seismometer pair which forms the pitch sensor. This then requires high gain feedback loops on the angular control loop downstream, which themselves are limited by their respective sensor noise at **number** Hz. This left over noise then leaks into the gravitational wave band between **number** and **number** Hz due to the inability to sharply roll off the control without interfering with control at lower frequencies.

add angular controls plot

The compact Beam Rotation Sensor (cBRS), described in the following, was designed to be an alternative angular sensor for the seismic isolation system with **number** times lower noise than the current sensors. With this decreased noise, the seismic isolation control loops can be tuned to significantly increase the performance of both the translational isolation, through decreased tilt contamination described in Section **??**, and directly the rotational isolation. Details of this follow in Section 3.2. This decreased residual rotation would then allow the angular control loops to be retuned, specifically decreasing the gain, to push the

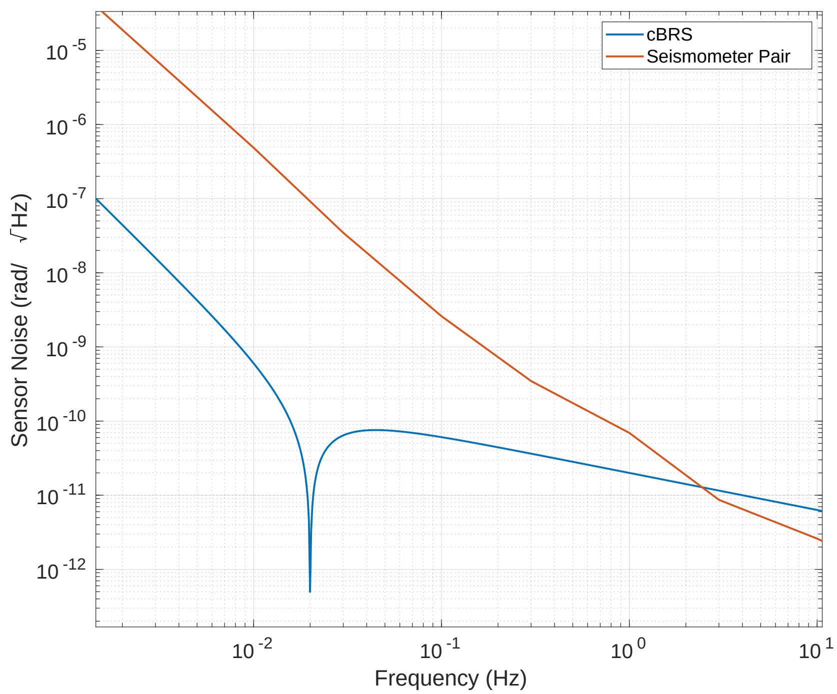

Figure 3.1

sensor noise leakage below the design sensitivity. **Need to check this.**

3.2 Isolation Scheme

Assuming that the isolation is limited by the noise of the in-band sensor, placing the lowest noise sensors on the second stage of the ISI would be expected to yield the lowest angular motion seen by the down stream control loops. With this in mind and the fact that the access to place new sensors is easier for the second stage, a control scheme was modeled which consists of the addition of an idealized cBRS (described in Section **??**) on stage 2. This model consisted of only two mechanical degrees of freedom, one horizontal translation and the rotational about the orthogonal horizontal axis.

The rotational control loop for stage 2 then consists of using the CPS between stage 1

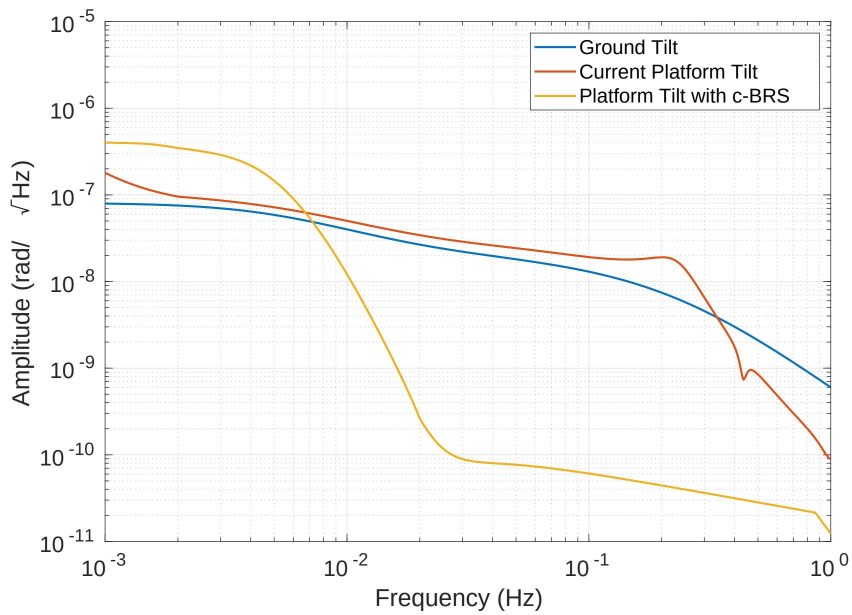

Figure 3.2

and stage 2 at low frequencies, the cBRS at frequencies between 3 mHz and 0.9 Hz, and the GS-13 pairs at frequencies above that. The blend frequencies were tuned to minimized the rms motion at low frequencies while maximizing the isolation at 0.1 Hz.

3.3 Mechanical System

Similar to the BRS described in Chapter 2, the compact Beam Rotation Sensor (cBRS), shown in Figure 3.4, consists of a 30-cm long cross hung from 10-15 μm thick beryllium-copper flexures and has an identical operating principle as the BRS. The cross shape of the balance decreases the sensitivity of the device to gradients in the local gravitational field while allowing for increased moment of inertia compared to a similarly sized beam.

This design yields a resonant frequency of $\sim$20 mHz limited the use of such a device to frequencies above this.

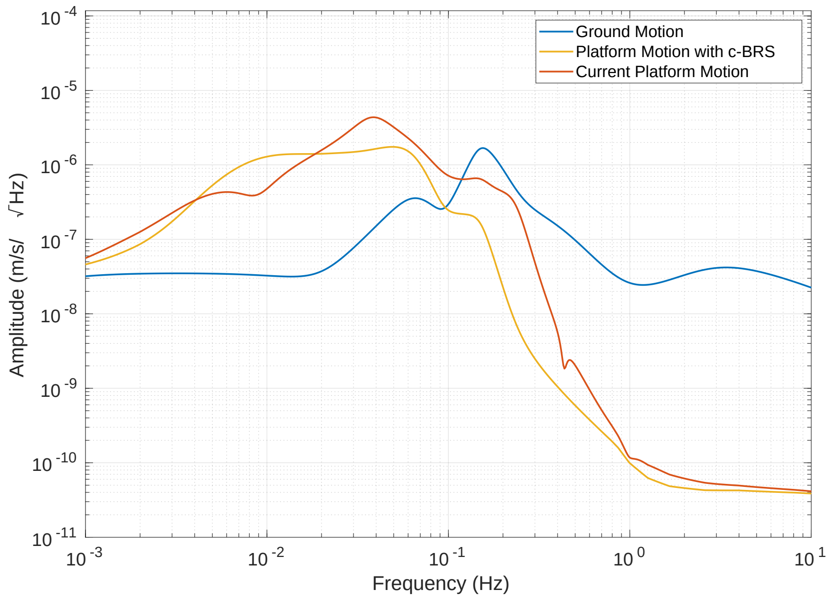

Figure 3.3

3.4 Interferometric Readout

In order to maintain the small size of the entire device, an interferometric readout was developed that consists of a Fabry-Perot cavity that is formed by a beamsplitter coated optical fiber and the full reflectance mirror placed on the bottom of the balance's end masses. The reflectance of this cavity is then monitored by employing a circulator to seperate the incoming and outgoing rays. As the cavity length changes the reflectence undergoes an interference pattern described by:

$$R = \frac{1}{1 + F\sin(\delta/2\lambda)} \tag{3.1}$$

include layout of cBRS optics

To linearize this readout, the optical fiber tip and collimating lens are placed on a translation stage that is driven by a piezo stack. The intensity of the reflected light is then fed

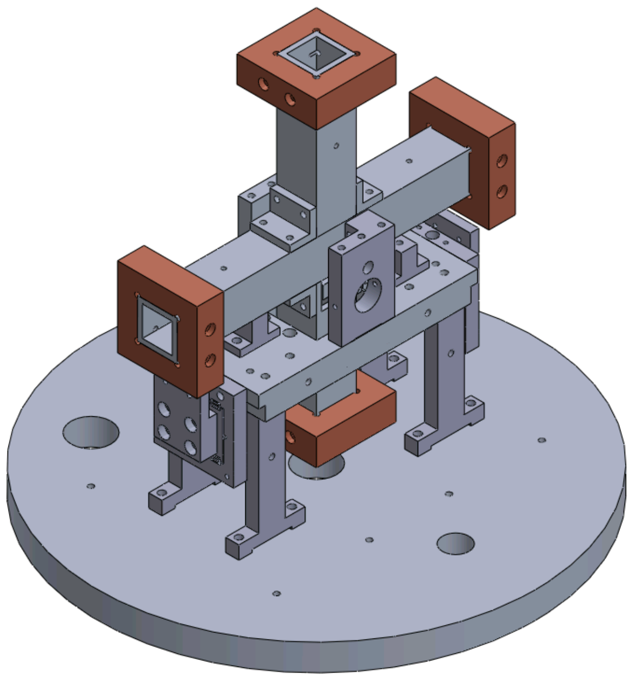

(a)

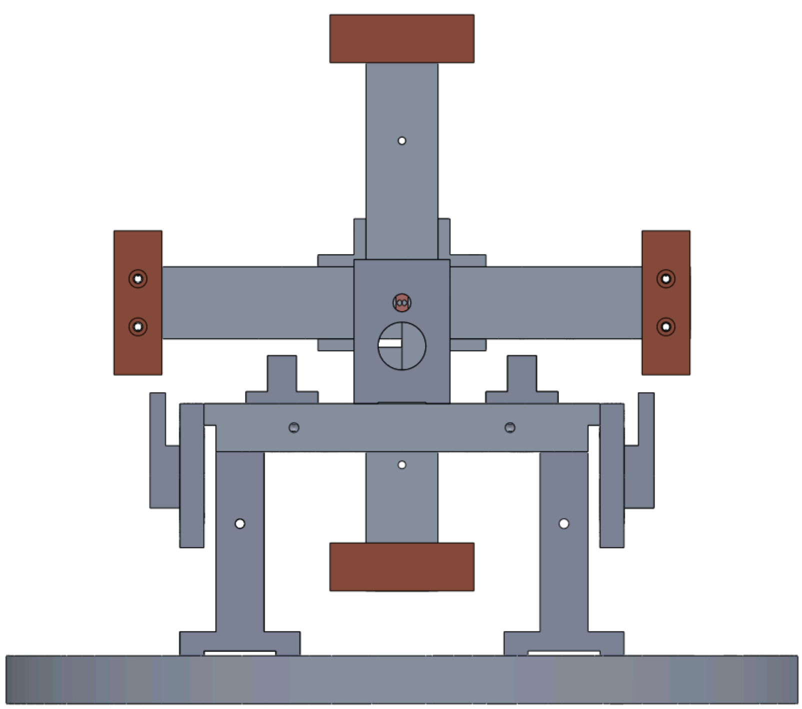

(b)

back to the piezos using a PID loop to hold the cavity length fixed. This allows the system to be seperated into two linear readouts, the interferometer output for small ranges above the unity gain frequency (UGF) of the loop and the control loop output for large motions below the UGF. The output of the device is then the sum of these two channels.

include table of PID parameters

include image of readout noise

3.5 Mass Adjustment

Through a variety of mechanisms, the devices described here can undergo long term drifts of the equilibrium position that can drive the beam balance past the dynamic range of the readout. To counteract this, a mass on the balance can be moved or added to shift the center of mass as such:

$$\Delta\theta = \frac{g}{\kappa} m r \tag{3.2}$$

where $\Delta\theta$ is the change in equilibrium angle, g is the gravitational acceleration, κ is the spring constant of the flexure, m is the mass added, and r is the distance from the mass and the pivot point.

While for the BRS the horizontal center of mass (COM) was designed to be tuned by hand, for the cBRS to operate in vacuum this must be done remotely and in an automated fashion. To achieve this a mass adjuster shown in Figure **??** consisting of a small aluminum mass on a fine pitched threaded rod is placed on the beam balance.

3.6 Controls

Similar to the BRS controls, the cBRS can be rung up do to environmental transients which can cause resonant motion in excess of the readout's dynamic range. To decrease these amplitudes, two capacitive actuators are placed under the end masses of the beam. These are actuated with low gain with the angular readout band passed around the resonant frequency.

3.7 Noise Performance

Chapter 4

APPLICATIONS

The development of these highly sensitive rotation sensors have opened up a few novel scientific avenues that have been explored and many that have not.

4.1 Geophysics

Seismic waves have six components, three translations and three rotations, however seismology has long neglected the rotational components due the lack of sensitive rotation sensors. Recent developments have begun to alleviated this issue with the advent of seismically relevant ring laser gyros. **cite Gryo** The BRSs described above join a small class of ground rotation sensors with high enough sensitivity at low frequency to allow for the use in seismology.

4.1.1 Rayleigh Wave Theory

Seismic waves can be broken into two classes: body waves and surface waves. In regard to surface waves there are two polarization, of the motion caused by a Love wave is constrained to the plane parallel with the surface of the medium while Rayleigh waves are constrained to a plane perpendicular the surface.

The plane wave solution of a Rayleigh wave has six components $(u_x, u_y, u_z, \theta_x, \theta_y, \theta_z)$ where u_i designated the translational motion in the ith direction while θ_i is the rotation about the ith axis. These can be described as with the following **cite seismic paper**

$$u_x(\mathbf{r},t) = \alpha sin(\zeta)cos(\psi)cos(\omega t - \mathbf{k}\cdot\mathbf{r}) \tag{4.1}$$

$$u_y(\mathbf{r},t) = \alpha sin(\zeta)sin(\psi)cos(\omega t - \mathbf{k}\cdot\mathbf{r}) \tag{4.2}$$

$$u_z(\mathbf{r},t) = \alpha cos(\zeta)cos(\omega t - \mathbf{k}\cdot\mathbf{r} + \pi/2) \tag{4.3}$$

$$\theta_x(\mathbf{r},t) = \frac{\partial u_z}{\partial y} = \alpha\kappa cos(\zeta)sin(\psi)cos(\omega t - \mathbf{k}\cdot\mathbf{r}) \tag{4.4}$$

$$\theta_y(\mathbf{r},t) = -\frac{\partial u_z}{\partial x} = -\alpha\kappa cos(\zeta)cos(\psi)cos(\omega t - \mathbf{k}\cdot\mathbf{r}) \tag{4.5}$$

$$\theta_z(\mathbf{r},t) = \frac{1}{2}\Big(\frac{\partial u_y}{\partial x} - \frac{\partial u_x}{\partial y}\Big) = 0 \tag{4.6}$$

where α is the amplitude, ζ is the ellipticity angle, ψ is the angle of incidence in the horizontal plane, ω is the frequency, and $\mathbf{k} = \kappa(\cos(\psi), \sin(\psi), 0)$ is the wavevector.

From these equations it can be seen that with a single seismic station with a traditional 3-axis seismometer, one can not measure all five parameters that define this wave field. Additionally, the horizontal components, u_x and u_y can contain contributions from co-propagating Love waves which further muddles ones ability to extract parameters.

4.1.2 Wave Field Parameter Extraction

With the combined measurements of the translational and rotational components at a single station, one can readily extract wavefield parameters that would otherwise be difficult to obtain, namely the phase velocity and the angle of incidence.

Seismic wave phase velocities are common observable which not only allows for understanding of Rayleigh wave propogation but can be inverted to yield tomographical structure profiles of the interior of the earth. **cite** The traditional method of extracting these is the exploit the time of arrival of a wave as it passes through an array of many seismometers. The analysis can be constrained to only the vertical channel which is insensitive to Love waves which could contaminate the measurements. However, this method requires many devices and effectively averages over the size of the array.

Alternatively, with measurements of the rotational components a point like measurement of the phase velocity can be made with three devices, a 3-component seismometer and two horizontal rotation sensors. This can be shown in the following equations:

$$v = \frac{\omega}{\kappa} = \frac{\dot{u}_z}{\theta_x}\sin(\psi) \tag{4.7}$$

$$v = \frac{\dot{u}_z}{\theta_y}\cos(\psi) \tag{4.8}$$

$$v = \frac{\dot{u}_z}{\sqrt{\theta_x^2 + \theta_y^2}} \tag{4.9}$$

where the dot represents the temporal derivative. Equations 4.7 and 4.8 can be utilized if a station has only one horizontal rotation sensor but requires independent determination of ψ. In contrast, Equation 4.9 contains only information from a single station.

In addition to the phase velocity, the angle of incidence can be determined with the following:

$$\psi = \arctan\left(\frac{\theta_x}{\theta_y}\right) \tag{4.10}$$

Although in theory, this can be measured using a single seismometer, Love wave contamination of the horizontal translational channels would distort any such measurement. As the horizontal rotational channels are insensitive to Love waves, they allow the extraction of ψ without such contamination.

4.1.3 Single Station Dispersion Measurements

Hanford Measurements

As described in Section 2.7, two BRSs were installed at LHO, one at each end station located 5.66 meters apart.

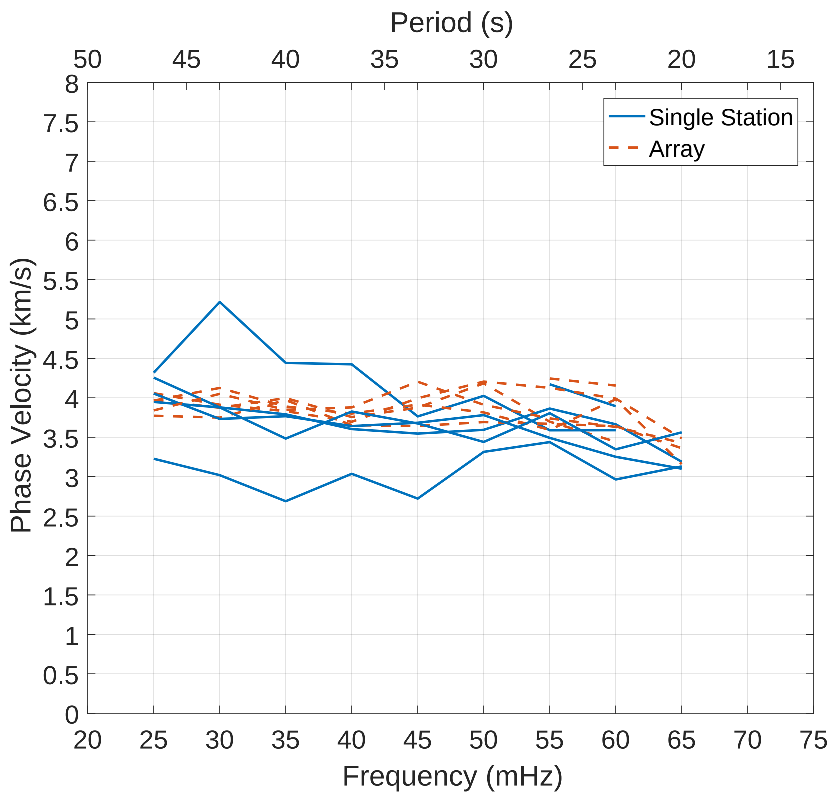

Figure 4.1: **cite tilt seismology**

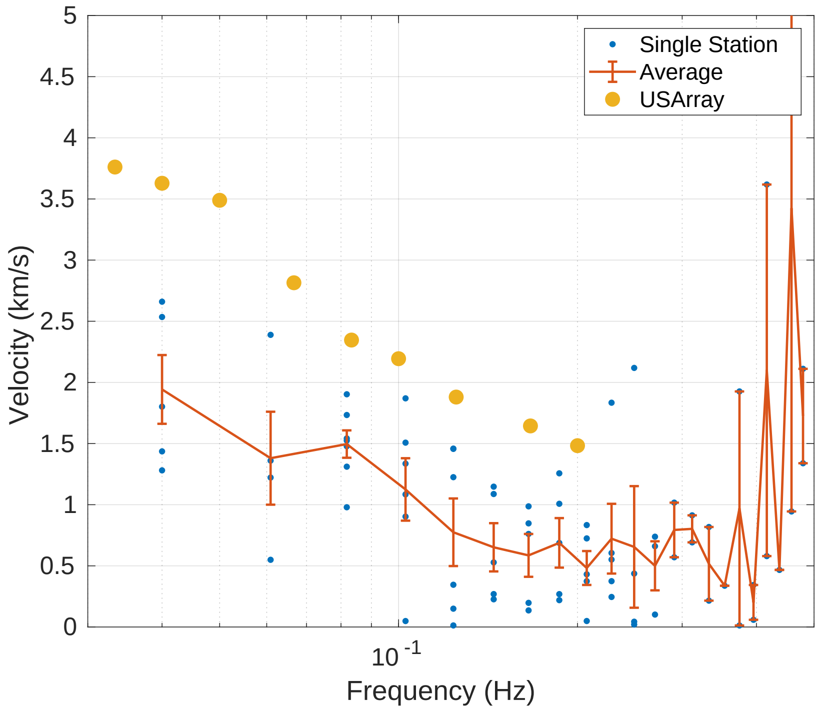

Figure 4.2

Livingston Measurements

4.2 Newtonian Noise

4.2.1 Theory

4.2.2 Observations

BIBLIOGRAPHY

[1] Aasi, J. et al. (2015). Advanced ligo. *Classical and Quantum Gravity*, 32(7):074001.

[2] B Arp, T., A Hagedorn, C., Schlamminger, S., and H Gundlach, J. (2013). A reference-beam autocollimator with nanoradian sensitivity from mhz to khz and dynamic range of 10(7.). *The Review of scientific instruments*, 84:095007.

[3] Belfi, J., Beverini, N., Carelli, G., Di Virgilio, A., Maccioni, E., Saccorotti, G., Stefani, F., and Velikoseltsev, A. (2012). Horizontal rotation signals detected by "g-pisa" ring laser for the mw = 9.0, march 2011, japan earthquake. *Journal of Seismology*, 16(4):767–776.

[4] Einstein, A. and Rosen, N. (1937). On gravitational wav es. *Journal of the Franklin Institute*, 223(1):43 – 54.

[5] et. al., S. (2016). First deep underground observation of rotational signals from an earthquake at teleseismic distance using a large ring laser gyroscope. *arXiv*.

[6] Haskell, N. A. (1953). The dispersion of surface waves on multilayered media. *Bulletin of the Seismological Society of America*, 43(1):17–34.

[7] Lantz, B., Schofield, R., O'Reilly, B., Clark, D. E., and DeBra, D. (2009). Review: Requirements for a ground rotation sensor to improve advanced ligo. *Bulletin of the Seismological Society of America*, 99(2B):980–989.

[8] Lee, W. H. K., Celebi, M., Todorovska, M. I., and Igel, H. (2009). Introduction to the special issue on rotational seismology and engineering applications. *Bulletin of the Seismological Society of America*, 99(2B):945–957.

[9] Legendre, C. P., Zhao, L., Huang, W.-G., and Huang, B.-S. (2015). Anisotropic rayleigh-wave phase velocities beneath northern vietnam. *Earth, Planets and Space*, 67(1):28.

[10] Lin, C.-J., Huang, H.-P., Pham, N. D., Liu, C.-C., Chi, W.-C., and Lee, W. H. K. (2011). Rotational motions for teleseismic surface waves. *Geophysical Research Letters*, 38(15):n/a–n/a. L15301.

[11] Lin, F.-C., Moschetti, M. P., and Ritzwoller, M. H. (2008). Surface wave tomography of the western united states from ambient seismic noise: Rayleigh and love wave phase velocity maps. *Geophysical Journal International*, 173(1):281.

[12] Maranó, S. and Fäh, D. (2014). Processing of translational and rotational motions of surface waves: Performance analysis and applications to single sensor and to array measurements. *Geophysical Journal International*, 196:317–339.

[13] Matichard, F. et al. (2015). Seismic isolation of advanced ligo: Review of strategy, instrumentation and performance. *Classical and Quantum Gravity*, 32(18):185003.

[14] Meier, T., Dietrich, K., Stöckhert, B., and Harjes, H. (2004). One-dimensional models of shear wave velocity for the eastern mediterranean obtained from the inversion of rayleigh wave phase velocities and tectonic implications. *Geophysical Journal International*, 156(1):45–58.

[15] Pancha, A., Webb, T. H., Stedman, G. E., McLeod, D. P., and Schreiber, K. U. (2000). Ring laser detection of rotations from teleseismic waves. *Geophysical Research Letters*, 27(21):3553–3556.

[16] Reinwald, M., Bernauer, M., Igel, H., and Donner, S. (2016). Improved finite-source inversion through joint measurements of rotational and translational ground motions: a numerical study. *Solid Earth*, 7(5):1467–1477.

[17] Venkateswara, K., Hagedorn, C. A., Gundlach, J. H., Kissel, J., Warner, J., Radkins, H., Shaffer, T., Lantz, B., Mittleman, R., Matichard, F., and Schofield, R. (2017). Subtracting tilt from a horizontal seismometer using a ground rotation sensor. *Bulletin of the Seismological Society of America*, 107(2):709–717.

[18] Venkateswara, K., Hagedorn, C. A., Turner, M. D., Arp, T., and Gundlach, J. H. (2014). A high-precision mechanical absolute-rotation sensor. *Review of Scientific Instruments*, 85(1).

[19] Weiss, R. (1972). Electromagnetically coupled broadband gravitational antenna. In *K.S. Thorne, "Gravitational radiation", 300 Years of Gravitation, S W Hawking and W Israel, pp 330–458*. University Press.

BIBLIOGRAPHY

[1] Aasi, J. et al. (2015). Advanced ligo. *Classical and Quantum Gravity*, 32(7):074001.

[2] B Arp, T., A Hagedorn, C., Schlamminger, S., and H Gundlach, J. (2013). A reference-beam autocollimator with nanoradian sensitivity from mhz to khz and dynamic range of 10(7.). *The Review of scientific instruments*, 84:095007.

[3] Belfi, J., Beverini, N., Carelli, G., Di Virgilio, A., Maccioni, E., Saccorotti, G., Stefani, F., and Velikoseltsev, A. (2012). Horizontal rotation signals detected by "g-pisa" ring laser for the mw = 9.0, march 2011, japan earthquake. *Journal of Seismology*, 16(4):767–776.

[4] Einstein, A. and Rosen, N. (1937). On gravitational wav es. *Journal of the Franklin Institute*, 223(1):43 – 54.

[5] et. al., S. (2016). First deep underground observation of rotational signals from an earthquake at teleseismic distance using a large ring laser gyroscope. *arXiv*.

[6] Haskell, N. A. (1953). The dispersion of surface waves on multilayered media. *Bulletin of the Seismological Society of America*, 43(1):17–34.

[7] Lantz, B., Schofield, R., O'Reilly, B., Clark, D. E., and DeBra, D. (2009). Review: Requirements for a ground rotation sensor to improve advanced ligo. *Bulletin of the Seismological Society of America*, 99(2B):980–989.

[8] Lee, W. H. K., Celebi, M., Todorovska, M. I., and Igel, H. (2009). Introduction to the special issue on rotational seismology and engineering applications. *Bulletin of the Seismological Society of America*, 99(2B):945–957.

[9] Legendre, C. P., Zhao, L., Huang, W.-G., and Huang, B.-S. (2015). Anisotropic rayleigh-wave phase velocities beneath northern vietnam. *Earth, Planets and Space*, 67(1):28.

[10] Lin, C.-J., Huang, H.-P., Pham, N. D., Liu, C.-C., Chi, W.-C., and Lee, W. H. K. (2011). Rotational motions for teleseismic surface waves. *Geophysical Research Letters*, 38(15):n/a–n/a. L15301.

[11] Lin, F.-C., Moschetti, M. P., and Ritzwoller, M. H. (2008). Surface wave tomography of the western united states from ambient seismic noise: Rayleigh and love wave phase velocity maps. *Geophysical Journal International*, 173(1):281.

[12] Maranó, S. and Fäh, D. (2014). Processing of translational and rotational motions of surface waves: Performance analysis and applications to single sensor and to array measurements. *Geophysical Journal International*, 196:317–339.

[13] Matichard, F. et al. (2015). Seismic isolation of advanced ligo: Review of strategy, instrumentation and performance. *Classical and Quantum Gravity*, 32(18):185003.

[14] Meier, T., Dietrich, K., Stöckhert, B., and Harjes, H. (2004). One-dimensional models of shear wave velocity for the eastern mediterranean obtained from the inversion of rayleigh wave phase velocities and tectonic implications. *Geophysical Journal International*, 156(1):45–58.

[15] Pancha, A., Webb, T. H., Stedman, G. E., McLeod, D. P., and Schreiber, K. U. (2000). Ring laser detection of rotations from teleseismic waves. *Geophysical Research Letters*, 27(21):3553–3556.

[16] Reinwald, M., Bernauer, M., Igel, H., and Donner, S. (2016). Improved finite-source inversion through joint measurements of rotational and translational ground motions: a numerical study. *Solid Earth*, 7(5):1467–1477.

[17] Venkateswara, K., Hagedorn, C. A., Gundlach, J. H., Kissel, J., Warner, J., Radkins, H., Shaffer, T., Lantz, B., Mittleman, R., Matichard, F., and Schofield, R. (2017). Subtracting tilt from a horizontal seismometer using a ground rotation sensor. *Bulletin of the Seismological Society of America*, 107(2):709–717.

[18] Venkateswara, K., Hagedorn, C. A., Turner, M. D., Arp, T., and Gundlach, J. H. (2014). A high-precision mechanical absolute-rotation sensor. *Review of Scientific Instruments*, 85(1).

[19] Weiss, R. (1972). Electromagnetically coupled broadband gravitational antenna. In *K.S. Thorne, "Gravitational radiation", 300 Years of Gravitation, S W Hawking and W Israel, pp 330–458*. University Press.